

Research Article

Transducer Field Imaging Using Acoustography

**Jaswinder S. Sandhu,¹ Robert W. Schoonover,² Joshua I. Weber,¹ J. Tawiah,¹
Vitaliy Kunin,¹ and Mark A. Anastasio²**

¹ Santec Systems, Inc., 2924 Malmo Drive, Arlington Heights, IL 60005, USA

² Department of Biomedical Engineering, Washington University in St. Louis, St. Louis, MO 63130, USA

Correspondence should be addressed to Jaswinder S. Sandhu, j-sandhu@santecsystems.com

Received 23 December 2011; Accepted 29 March 2012

Academic Editor: Jafar Saniie

Copyright © 2012 Jaswinder S. Sandhu et al. This is an open access article distributed under the Creative Commons Attribution License, which permits unrestricted use, distribution, and reproduction in any medium, provided the original work is properly cited.

A common current practice for transducer field mapping is to scan, point-by-point, a hydrophone element in a 2D raster at various distances from the transducer radiating surface. This approach is tedious, requiring hours of scanning time to generate full cross-sectional and/or axial field distributions. Moreover, the lateral resolution of the field distribution image is dependent on the indexing steps between data points. Acoustography is an imaging process in which an acousto-optical (AO) area sensor is employed to record the intensity of an ultrasound wavefield on a two-dimensional plane. This paper reports on the application of acoustography as a simple but practical method for assessing transducer field characteristics. A case study performed on a commercial transducer is reported, where the radiated fields are imaged using acoustography and compared to the corresponding quantities that are predicted numerically.

1. Introduction

An important aspect of transducer quality control is to assess the radiated ultrasonic field characteristics, which can be affected by factors such as piezoelectric element misalignment with respect to transducer housing, material inhomogeneity, lack of bonding, electrode design and contact placement, acoustic lens quality, and wear plate uniformity and adhesion, to mention a few. A common practice for assessing beam characteristics is to scan a small hydrophone element point-by-point in a plane perpendicular to the transducer's radiation axis [1, 2]. This generates a 2D cross-sectional field distribution at a given distance away from the transducer's radiating surface. To generate a 3D field distribution, 2D cross-sectional distributions are generated at increasing distances along the radiation axis. Hydrophone scanning is slow and tedious, requiring many hours of scanning time to generate the complete field characteristics of the transducer. Moreover, the lateral resolution of the hydrophone scanning method is dependent on the indexing steps between data points as well as the hydrophone element size.

Acoustography [3, 4] is a full-field ultrasonic imaging process wherein an acousto-optical (AO) area sensor is employed to convert ultrasound into a visual image in real time. The AO sensor converts ultrasound energy directly into a visual image by virtue of the inherent acousto-optic effect in our proprietary liquid crystal (LC) or "mesophase" material contained in the AO sensor [3–5]. Theoretical and experimental investigations into the dynamics of liquid crystal devices have been performed to assess the role of geometrical and liquid crystal properties in similar devices [6, 7]. Liquid crystal devices utilizing the AO effect have found utility in acoustic holography [8], medical imaging [9], optical devices [10], and the inspection of composites [11].

In this paper, we report on the application of acoustography for mapping transducer fields. Since it can yield high spatial-resolution recordings of a 2D cross-sectional field distribution without the need for mechanical scanning, acoustography represents a simple and practical method for this application. Experimental studies are conducted in which acoustography is employed to map the fields produced by a commercial transducer at a collection of distances along the transducer's radiation axis. These recordings are compared

to estimates of the fields obtained by numerically solving the associated Rayleigh diffraction integral.

2. Background: Basic Principles of AO Sensors

In the AO sensor used in this work, the LC molecules are initially arranged to be parallel to each other but perpendicular to the confining substrates; confining substrates are acoustically transparent, but one of the substrates is also optically transparent. In this configuration of the molecules, the LC material behaves like a slab of a uniaxial, positive birefringent crystal with optic axis parallel to the LC molecular alignment direction (\underline{n}). For such an LC layer, the optical behavior (i.e., brightness change, T) under polarized light can be described by [12]:

$$T = \sin^2 \left[\left(\frac{2\pi d}{\lambda} \right) \cdot (n_{\parallel} - n_{\perp}) \cdot \sin^2 \theta(I) \right], \quad (1)$$

where d is LC layer thickness; λ is wavelength of light; n_{\parallel} is refractive index of LC along the optic axis (\underline{n}); n_{\perp} is refractive index of LC perpendicular to optic axis (\underline{n}); $\theta(I)$ is ultrasonically induced tilt angle of the LC molecules that is a function of the ultrasonic intensity I .

In the absence of an ultrasound field, the molecular tilt angle, θ , is zero, and the AO sensor is uniformly dark across the field of view. However, when an area of the AO sensor is exposed to an ultrasonic field, the LC molecules experience a torque [13], which tilts the LC molecules in the ultrasonically exposed region of the AO sensor. As a result, the ultrasonically exposed area of the AO sensor appears bright. Figure 1 illustrates this process. The local induced brightness level of the AO sensor is related to the local ultrasonic intensity [13]; therefore, an ultrasonic intensity image can be created from the visual image of the AO sensor.

The lateral resolution in acoustography is very high because the visual image is created by the local interaction between the ultrasound field and the (~ 2 nanometer) LC molecules. In practice, the transverse resolution of this method is limited by the optical camera used to image the AO sensor. For this study, an optical system with 0.31 mm pixel size was chosen; however, higher-resolution optical cameras may be used when the application warrants it. The contrast resolution in acoustography depends on the AO sensor's acousto-optic transfer curve [6, 8], which is analogous to the characteristic curve of an X-ray detector. The AO transfer curve expresses the relationship between ultrasonic intensity and the corresponding optical density (brightness level).

3. Methods

3.1. Imaging System. Figure 2 displays an overhead view of the acoustography imaging system. The system consists of a water-immersion tank with dimensions 36''(L) \times 36''(W) \times 12''(D); a 1'' diameter flat circular test transducer (GE Inspection Technologies) suspended in the water tank; a 5'' \times 5'' area AO sensor; a digital video camera (Basler A311, not shown) housed in the Optics Box. The optical system has an effective pixel size of 0.31 mm \times 0.31 mm. The test transducer was attached to a moveable slide, where the position

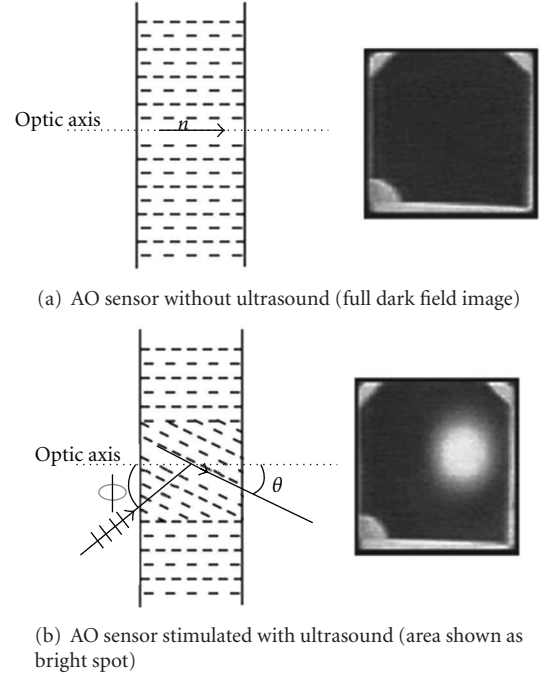


FIGURE 1: In panel (a), a schematic of the AO sensor before insonification by an ultrasound field is shown alongside an image of the AO sensor, when the LC molecules are aligned along the optical axis. In panel (b), a schematic of the AO sensor after insonification by an ultrasound field is shown alongside an image of the AO sensor, when the LC molecules have been perturbed by an ultrasound field.

of the movable slide could be set with an accuracy of ± 1 mm with respect to the position of the AO sensor. The beam angle of the test transducer was set with an accuracy of better than 0.5° .

3.2. Experimental Studies. For a flat, circular transducer, such as the one used in this experiment, the ultrasonic intensity along the central axis of the transducer can be expressed as [14]

$$\frac{I(z)}{I(0)} = \sin^2 \left[\frac{\pi}{\lambda} \left(\sqrt{r^2 + z^2} - z \right) \right], \quad (2)$$

where $I(0)$ is the maximum intensity, $I(z)$ is the intensity at distance z from the transducer radiating surface, r is radius of the transducer radiating element, and λ is the acoustic wavelength in water. Two-dimensional images of the radiation pattern of the cylindrical transducer were made at four distances, as measured along the central axis of the transducer. Each measurement distance corresponded to either a minimum or maximum of the intensity along the axis (see Figure 3), or a point in the far-field of the transducer. The transition between the near-field and the far-field for this transducer was calculated to be at 35.3 cm.

The nominal frequency of the transducer was 3.5 MHz. However, the transducer was operated at 3.3 MHz to match the operating frequency of the AO sensor. The transducer beam angle was set at 21° with respect to the AO sensor

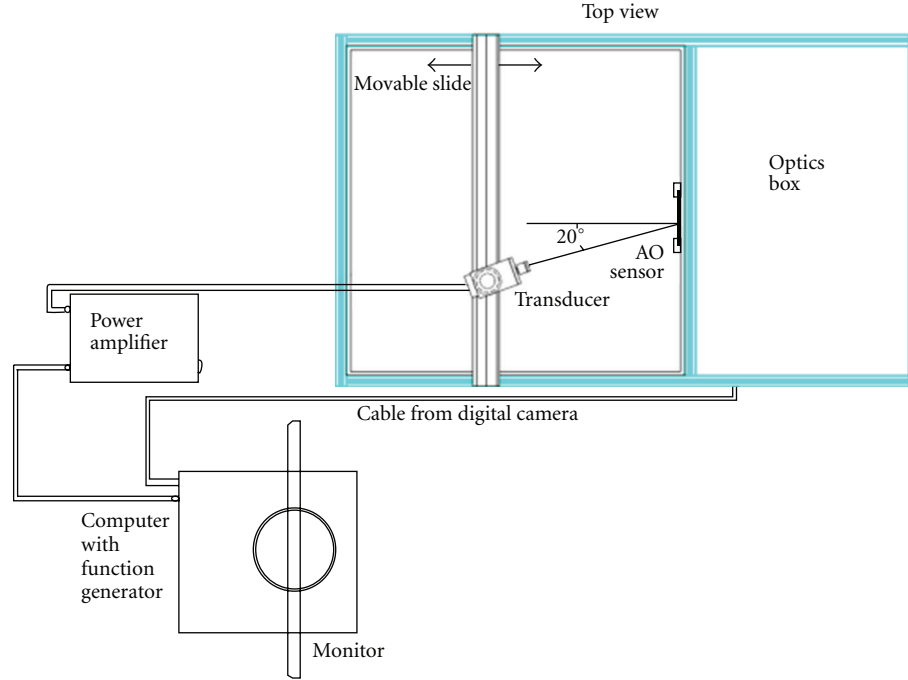


FIGURE 2: An overhead view of the acoustic imaging system.

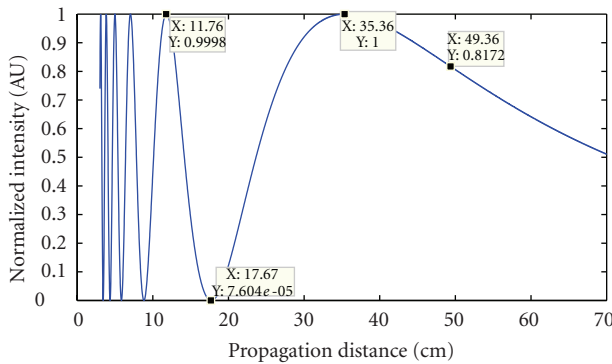


FIGURE 3: Intensity profile along the central radiation axis of a 1'' diameter transducer element operated at 3.3 MHz.

normal, to avoid reverberations between the AO sensor and the transducer's radiating surface. The transducer was energized using a continuous wave (CW) signal.

For each measurement distance, the intensity map on the AO sensor was captured after less than 10 seconds of insonification. Image capture and processing by the camera system was performed in 30 seconds. The AO sensor has a reset time (to realign the LC molecules) of less than 5 seconds. Thus, the ultrasound intensity at >22,000 distinct spatial positions (142×156 array) was measured in less than 35 seconds total.

3.3. Computer-Simulation Studies. Simulations of the ultrasonic field produced by a 1'' transducer were also performed to corroborate the images acquired in the experimental

studies. The simulations, performed using the DREAM Toolbox for MATLAB [15], calculated the spatial impulse response of a 0.95'' diameter transducer on a plane rotated by 21° with respect to the central axis of the transducer, a distance z away (where z corresponds to the various measurement distances). The pixel size was chosen to be the same as the effective pixel size of the AO sensor + optical system: $0.31 \text{ mm} \times 0.31 \text{ mm}$. The choice of 0.95'' for the transducer diameter was chosen to best match the experimental data. The spatial impulse response was a $2D \times 1D$ signal (two spatial dimensions to represent the measurement plane and one temporal dimension to represent the time-varying ultrasound field). The discrete Fourier transform of the resulting time series at each pixel in the measurement plane was computed by use of the fast Fourier transform algorithm. The element of the discrete Fourier transform, most closely corresponding to 3.3 MHz at that pixel, was selected. The resulting 2D data, corresponding to a monochromatic ultrasound field at 3.3 MHz on the measurement plane, were then squared to represent the ultrasound intensity. The simulations assume a perfectly flat transducer with specified diameter.

4. Experimental Results

4.1. Experimental and Simulated Images. The first column of Figure 4 displays the ultrasonic field maps recorded by use of the AO sensor in the experimental studies. Specifically, the images depict the field intensity distributions on planes located at distances $z = 11.76 \text{ cm}$ (panel (a)), 17.67 cm (panel (d)), 35.36 cm (panel (g)), and 49.36 cm (panel (j)) from the transducer face along the radiation axis.

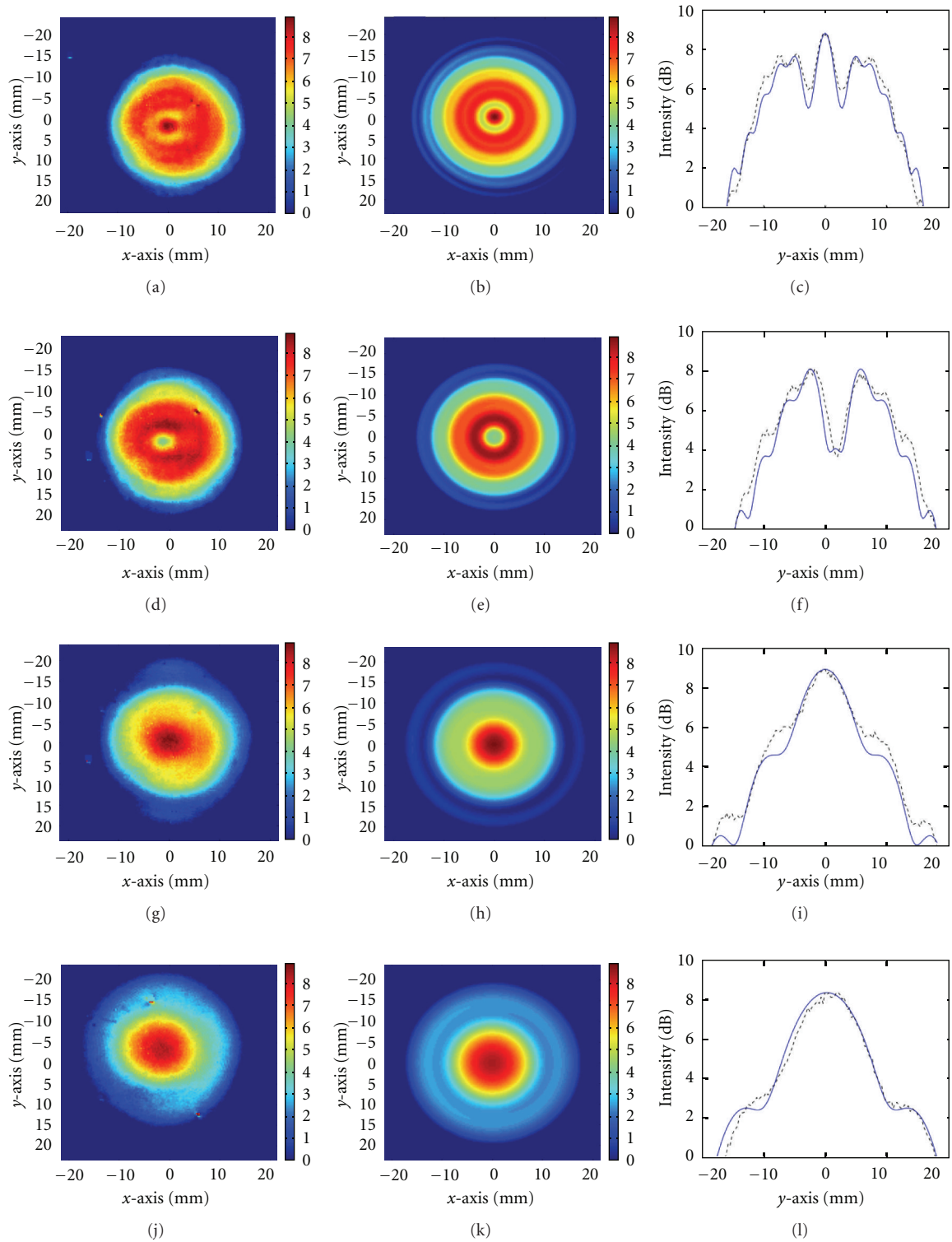


FIGURE 4: Images of the experimentally determined transducer radiation patterns are shown in the first column. In the second column, theoretically determined transducer radiation patterns are shown. Line plots through the center of the experimental data (black dashed lines) and the theoretical data (blue solid lines) are shown in the third column. The first row corresponds to a propagation distance of 11.76 cm (the location of an intensity maximum on the optical axis in the near zone). The second row corresponds to a propagation distance of 17.67 cm (the location of an intensity minimum on the optical axis in the near zone). The third row corresponds to a propagation distance of 35.36 cm (the near-zone/far-zone transition distance). The fourth row corresponds to a propagation distance of 49.36 cm (a distance in the far zone).

The distances were chosen based on the on-axis intensity profile in Figure 3. The ultrasound intensity in these images was displayed in decibels.

The corresponding simulated intensity images are displayed in the middle column of Figure 4. The simulated intensity data was scaled so that the peak intensity in each simulation matched the peak intensity in the corresponding experimental data. Plots along the y -axis ($x = 0$) of both the experimental (black dashed lines) and theoretical (blue solid lines) results are shown in panels (c), (f), (i), and (l) of Figure 4.

4.2. Discussion of Results. One notes that there is an overall qualitative agreement between the intensity patterns generated through simulation and those obtained with the AO sensor. Comparisons of the intensities in the first and second columns of Figure 4 show strong agreement in predicting the ring structure in the near-zone measurements (first and second rows). For example, in Figure 4(c), the experimental measurements illustrate the same peak-trough-shoulder structure as the theoretical results do for $z = 11.76$ cm. The experimental data also matches the theoretical model in predicting the depth of the trough ($y = 2$ mm) between the two intensity peaks ($y = -3$ mm and $y = 5$ mm) in Figure 4(f) ($z = 17.67$ mm) as well as the predicting the presence of the intensity shoulders at $y = 9$ mm and $y = 14$ mm. The height of the shoulders is slightly underestimated by the simulation results, however. In Figures 4(i) and 4(l), one notes that the simulation matches the experimental results in predicting the width of the radiation pattern as well as predicting the intensity shoulder at $y = \pm 10$ mm in panel (i). The simulation underestimates that shoulder height, however.

The quantitative agreement between the two results may be improved upon through better modeling of the dynamics of the ultrasound field in the AO sensor. The transmission of the ultrasound field through the substrate and into the LC layer of the AO sensor is not accounted for in this analysis. Because of the large speed-of-sound mismatch between the substrate layer (~ 5000 m/s) and water (~ 1500 m/s), the transmission of various components of the angular spectrum [16] of the ultrasound field can vary greatly. By accounting for the transmission of sound through the medium, better quantitative accuracy will be achieved.

5. Conclusion

The possibility of applying acoustography to provide a simple but practical tool for mapping ultrasonic fields radiated from ultrasonic transducers has been demonstrated. Since acoustography does not require elaborate mechanical scanning equipment, it is suitable for routine use for quality assessment of transducer fields. The latter capability may be particularly important for calibration of phased array systems, which are being used more and more for nondestructive testing. Other benefits from acoustography have also been demonstrated: each intensity map took <35 seconds compared to hours using current conventional scanning techniques and methods; the entire procedure is user friendly and can be performed by low-skilled operators;

the method does not require calibration of the measurement device.

Future plans include a more indepth, head-to-head comparison and validation study of acoustography against the ball reflector method. This will remove any discrepancies that result from simulation modeling errors. In addition, refinement of the process will be pursued including automation, software development, and improved data analysis by obtaining the AO 2D cross-sectional fields and being able to generate true 3D axial profiles using frame-grabbing video output data. This is a distinct advantage over the convention ball reflector method, where the lateral resolution is primarily determined by the indexing step size. Fine indexing steps are required to achieve high resolution but that greatly increases the scan time required to map the ultrasound field. Further improvements in the image processing and analysis will also be pursued to account for the heterogeneous structure of the AO sensor.

Acknowledgment

R.W. Schoonover and M. A. Anastasio acknowledge the support from the National Institute of Health (NIH) awards EB010049 and EB009715.

References

- [1] P. G. Kenny, J. J. Gruber, and J. M. Smith, "Ultrasonic transducer characterization," *Materials Evaluation*, vol. 45, no. 6, pp. 730–735, 1987.
- [2] R. Lal and D. K. Das-Gupta, "Characterization of ultrasonic transducers," *IEEE transactions on electrical insulation*, vol. 24, no. 3, pp. 473–480, 1989.
- [3] J. S. Sandhu, "Acoustography," in *Special Nondestructive Testing Methods, Nondestructive Testing Handbook*, P. O. Moore and P. McIntire, Eds., vol. 9, pp. 278–284, American Society for Nondestructive Testing, Columbus, Ohio, USA, 2nd edition, 1995.
- [4] J. S. Sandhu, "Acoustography: a new imaging technique and its applications to nondestructive evaluation," *Materials Evaluation*, vol. 46, pp. 608–613, 1988.
- [5] O. A. Kapustina, "Acoustooptical phenomena in liquid crystals," *Molecular Crystals & Liquid Crystals*, vol. 112, pp. 1–164, 1984.
- [6] A. P. Malanoski, V. A. Greanya, B. T. Weslowski, M. S. Spector, J. V. Selinger, and R. Shashidhar, "Theory of the acoustic realignment of nematic liquid crystals," *Physical Review E*, vol. 69, no. 2, Article ID 021705, 2004.
- [7] V. A. Greanya, A. P. Malanoski, B. T. Weslowski, M. S. Spector, and J. V. Selinger, "Dynamics of the acousto-optic effect in a nematic liquid crystal," *Liquid Crystals*, vol. 32, no. 7, pp. 933–941, 2005.
- [8] G. L. Rodríguez, J. Weber, J. S. Sandhu, and M. A. Anastasio, "Feasibility study of complex wavefield retrieval in off-axis acoustic holography employing an acousto-optic sensor," *Ultrasonics*, vol. 51, no. 8, pp. 847–852, 2011.
- [9] J. S. Sandhu, R. A. Schmidt, and P. J. La Rivière, "Full-field acoustomammography using an acousto-optic sensor," *Medical Physics*, vol. 36, no. 6, pp. 2324–2327, 2009.
- [10] Y. J. Liu, X. Ding, S. C. S. Lin, J. Shi, I. K. Chiang, and T. J. Huang, "Surface acoustic wave driven light shutters using

- polymer-dispersed liquid crystals,” *Advanced Materials*, vol. 23, no. 14, pp. 1656–1659, 2011.
- [11] J. S. Sandhu, H. Wang, and W. J. Popek, “Acoustography for rapid ultrasonic inspection of composites,” in *Nondestructive Evaluation of Materials and Composites*, Proceedings of SPIE, pp. 117–124, December 1996.
 - [12] M. Born and E. Wolf, *Principles of Optics*, Pergamon Press, New York, NY, USA, 1987.
 - [13] J. S. Sandhu, H. Wang, and W. J. Popek, “Liquid crystal based acoustic imaging,” in *Liquid Crystal Materials, Devices and Flat Panel Displays*, R. Shashidhar and B. Gnade, Eds., vol. 3955 of *Proceedings of SPIE*, pp. 94–108, January 2000.
 - [14] L. E. Kinsler, A. R. Frey, A. B. Coppens, and J. V. Sanders, *Fundamentals of Acoustics*, Wiley, 1999.
 - [15] F. Lingvall, T. Olofsson, and T. Stepinski, “Synthetic aperture imaging using sources with finite aperture: deconvolution of the spatial impulse response,” *Journal of the Acoustical Society of America*, vol. 114, no. 1, pp. 225–234, 2003.
 - [16] L. Mandel and E. Wolf, *Optical Coherence and Quantum Optics*, Cambridge University Press, 1995.

